A Greedy Depth-Seeking Behavior for Energy-Efficient Transits by an Autonomous Underwater Vehicle

Raymond Young, Sophia Merrifield, Mark Anderson, Matthew Mazloff, and Eric Terrill

***Abstract*—An energy saving behavior is presented for autonomous underwater vehicles (AUVs) that uses greedy control decisions to take advantage of vertical gradients in ocean currents. The behavior relies on a dynamic vehicle model for motion and power consumption and environmental information that can be realistically obtained and processed onboard. Vehicle model parameters are consistent with a 12.75-in-diameter propeller-driven AUV. Simulation results are presented using a two-year tidally resolving ocean circulation model over three spatially distinct transits in the Southern California Bight. The energy saving behavior is compared to the common practice of transiting at fixed depth, as well as a "best case" scenario in which a vehicle has knowledge of the full-depth ocean current profile at its local position. The proposed behavior saves between 3% and 10% in energy expenditure depending on the vehicle's initial launch depth. On average, it is most efficient to initialize the vehicle at depths corresponding to the base of the surface oceanic mixed layer. Finally, a reduced order approximation of the optimal planning solution shows that the vehicle's depth choices oscillate with dominant tidal constituents for the region.**

***Index Terms*—Depth optimization, energy optimal, ocean currents and tides, path planning, simulation.**

I. Introduction

AUTONOMOUS underwater vehicles (AUVs) often operate in environments where the magnitude of ocean currents is on the same order as, or exceeds, vehicle speeds [1]. In these environments, currents will significantly affect an AUV's ability to navigate efficiently, which has motivated many studies on optimal path planning [2]. Optimal planning algorithms allow a vehicle to take advantage of the features of the environment to improve transit time and/or energy consumption [3], [4], [5].

Previous studies, in simulation, have demonstrated algorithms that solve the optimal planning problem for completeness (a solution will be found if it exists) and global optimality (see, e.g., [6] and [7]). These algorithms are computationally expensive and difficult to scale to 3-D and time-varying environments. In addition, these algorithms require complete environmental information such as synthetic current fields [3], large-scale ocean models [4], or model forecasts [8]. Due to the complexity of ocean conditions across a range of spatial and temporal scales, model forecasts tend to lose skill over one to two days. For example, Hoteit et al. [9] found that initial conditions could only provide skill in reproducing observed surface currents for about 18 h.

A common approach is to discretize and solve the path planning problem using graph search algorithms (e.g., Dijkstra's algorithm [10], A* [11], and rapidly exploring random trees (RRT) [12]). Early work on the 2-D time-invariant case focused on the exploitation of horizontal variability in ocean currents. In [3], A* was implemented on a uniform grid through simulated current fields to investigate energy savings with respect to eddy length scales. Rao and Williams [4] extended RRTs into an ocean environment by heuristically biasing growth of the tree toward helpful ocean currents. More recently, Kularatne et al. [6] have updated the A* implementation for AUVs with realistic cost functions and a graph construction that explicitly allows for time-varying currents. They [6] also parameterized grid discretization and connectedness to provide smooth paths and sufficient variability in speed selection. However, both the memory and runtime complexity of their algorithm scales poorly with both parameters and with the inclusion of depth.

Other algorithms solve the path planning problem in the continuous domain. Davis et al. [1] developed a method for a 2-D static environment based on the calculus of variations for time-optimal trajectories. Lolla et al. [7] first developed level set methods to find provably time-optimal paths in a 2-D time-varying environment. Kulkarni and Lermusiaux [8] extended these methods to a 3-D environment, Subramani et al. [13] applied level sets to propelled AUVs with an energy cost function (but in 2-D), and Doshi et al. [14] used level sets to find the Pareto front for a tradeoff between time-optimal and energy-optimal paths. This series of papers provides perhaps the most robust methodology for solving the optimal path planning problem, but it comes with a significant computational cost. For the 3-D time-optimal solution in a realistic current environment,

Manuscript received 4 October 2023; revised 17 January 2024, 26 March 2024, and 11 June 2024; accepted 21 June 2024. Date of publication 9 September 2024; date of current version 15 October 2024. The work of Raymond Young was supported by the U.S. Department of Defense through the National Defense Science and Engineering Graduate Fellowship Program. *(Corresponding author: Raymond Young.)*

Associate Editor: W. He.

Raymond Young, Sophia Merrifield, Matthew Mazloff, and Eric Terrill are with the Scripps Institution of Oceanography, University of California San Diego, San Diego, CA 92093 USA (e-mail: ray011@ucsd.edu; smerrifield@ucsd.edu; mmazloff@ucsd.edu; eterrill@ucsd.edu).

Mark Anderson is with the Jacobs School of Engineering, University of California San Diego, San Diego, CA 92093 USA (e-mail: m3anderson@ucsd.edu).

Digital Object Identifier 10.1109/JOE.2024.3429610

the computation time[1] for a mission with a completion time of 3.84 days was approximately 109 min [8]. While this is an acceptable planning to execution time ratio for operational work, it is not scalable to a study that considers many different initial and terminal state pairs, or a long time series of initial conditions. Finally, Lee et al. [15] developed a hierarchical planning algorithm in time-dependent flows to bridge the gap between discrete and continuous methods.

In parallel with research on globally optimal algorithms in simulation, significant work has been done to advance the onboard capabilities of marine robots. The focus of these studies is to dynamically replan a vehicle's path, often for the purpose of obstacle avoidance [16]. Fu-Guang et al. [17] introduced a local obstacle avoidance behavior for AUVs based on virtual potential fields [18], which solves the problem of being stuck in local minima behind obstacles. Leveraging more recent developments in machine learning, Yang et al. [19] created an obstacle avoidance algorithm for AUVs that considers ocean currents and dynamic obstacles using reinforcement learning, and Guerrero-González et al. [20] used biologically inspired neural networks for tracking and obstacle avoidance. Some obstacle avoidance algorithms have been successfully demonstrated onboard. For surface vehicles, Cole et al. [21] demonstrated obstacle avoidance with automatic information system detection and Benjamin et al. [22] implemented an algorithm that used light imaging, detection, and ranging to detect obstacles. In contrast, there have been few studies focused on the development of onboard behaviors for time/energy efficiency. Some limited examples include [1] that proposed a local steering rule to handle time-dependent currents based on insights from their global solution in a stationary environment, [23] that developed a behavior based on sensing current profiles from a long-range horizontal acoustic Doppler current profiler (ADCP) for time-optimal path planning over short missions [O(100 m)] in turbulent flows, and [24] that demonstrated a behavior to dynamically adjust propeller speeds for energy-efficient transits in level flight.

To the authors' knowledge, an onboard method that optimizes an AUV's depth to improve efficiency does not exist. To address this gap, we propose an autonomous behavior that enables dynamic depth seeking and changes in speed while transiting along a prescribed waypoint course. The behavior directly extends the 1-D method from [24] to 2-D, and it is based on the greedy minimization of power consumption per unit distance. While along/cross components of the current relative to the vehicle's course are considered in modeling AUV speed and power consumption, our method focuses on how currents change with depth. This choice is motivated by 1) sensing capabilities of AUVs in operation today, which have been deployed with upward- and downward-facing ADCPs [25], and 2) a focus on long-duration deployments [O(100 km)] over which the horizontal scales of variability in ocean currents can be much larger when compared to the vertical. The behavior is readily available for onboard implementation as it does not require full domain knowledge of the ocean currents. In addition, the behavior can be simulated quickly, in much less than 1 s per 100 km transit, which allows us to study the statistical relationship between the environment and path planning results across many simulations. In this study, results are presented for simulated transits in the Southern California Bight. The simulated AUV has parameters that are consistent with a REMUS 600 [25].

The rest of this article is organized as follows. In Section II, the ocean currents in Southern California are analyzed from a physical oceanographic perspective to understand what features can be exploited for energy savings. Section III describes the methods used to simulate the AUV and defines the energy saving behavior. Section IV summarizes the statistical results of energy consumption on spatially distinct transits simulated over a two-year window of initial start times. Finally, Section V concludes this article.

II. Environmental Model

This section provides a description of ocean currents in the Southern California Bight. We first describe the oceanographic model used in this study and select three transects for simulation. Next, we discuss the effects of tidal currents in the region. Finally, we examine ocean current features in both depth and along-track dimensions and how they are modulated by tides. Together, these analyses motivate a depth-seeking behavior by an AUV for improved efficiency.

A. Model Description

The ocean current model used in this study is a Regional MITgcm simulation of the California Current Region [26]. The regional model provides two years (2016–2017) of current vectors with hourly time resolution, approximately 1.8-km horizontal resolution, and variable depth resolution (1 m at the surface decreasing to 35 m at 600 m). It is forced with the HYbrid Coordinate Ocean Model plus Navy Coupled Data Assimilation at the ocean boundary and the fifth generation of European Centre for Medium-Range Weather Forecasts atmospheric reanalysis (ERA5) at the air–sea boundary. It includes local and remote tidal forcing. This model is unique with its inclusion of remotely forced internal wave energy at the boundary, which is shown to produce realistic high-frequency ocean variability. These dynamics are underestimated and/or missed in global ocean models that have previously been the focus of realistic path planning examples (see, e.g., [4]). This model was validated with data from tide gauges, stationary moorings, and satellite altimetry. A full description and validation of the model is provided in [26].

B. Transect Choices

Environmental analysis and subsequent simulation results focus on three transects that will be referred to as "Off Shore," "Cross Shore," and "Along Shore," as summarized in Table I. Each transect lies in the Southern California Bight, shown in Fig. 1, and was chosen to provide spatial variability between simulations.

[1]Calculations in [8] were implemented in MATLAB on a quad-core Intel i7-4790 CPU at 3.60 GHz.

TABLE I
TRANSECT SPECIFICS

Name	**Start** (deg N, deg W)	**End** (deg N, deg W)	**Length** [km]
Off Shore	(32.2991, 118.7957)	(33.3771, 118.7957)	119.55
Cross Shore	(33.1810, 118.7987)	(33.1810, 117.4864)	122.39
Along Shore	(32.9137, 117.3659)	(33.5500, 118.2000)	105.00

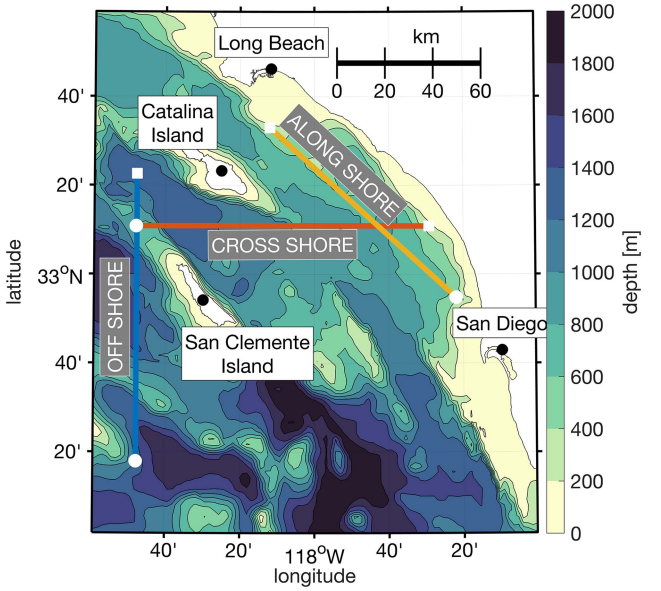

Fig. 1. Map of the Southern California Bight with three transects of interest. The start and end points of each transect are denoted by white circles and squares, respectively. Each of these paths is used in the environmental characterization as well as for the simulated vehicle missions.

The Off Shore transect was chosen to be in deep water where vehicle operating depths are not influenced by bathymetry. The Cross Shore transect was chosen to examine the effects on vehicle performance resulting from channel-intensified currents between Catalina and San Clemente islands. For most of the transect, the vehicle is uninhibited by bathymetry, until the last 20 km when it approaches the coastline. The Along Shore transect was chosen to examine the impacts of coastal currents influenced by shallow bathymetry.

C. Tidal Contributions

Tidal currents in the Southern California Bight are evaluated for each transect through spectral analysis. We examine the time series of vertical profiles of currents from three virtual moorings (VMs). Each VM is constructed as a 2-D (depth and time) slice of model output at the (latitude, longitude) grid point nearest to each transect midpoint. We will refer to "surface currents" as the time series at each VM that has been averaged in depth over model bins between the surface and 50 m.

At each depth, a power spectrum is computed according to Welch's method [27] with 30-day segments that overlap by 50%. These spectra are annotated in Fig. 2(a)–(c) with four dominant tidal constituents (O1, K1, M2, S2) in the region. While the currents at each VM are more energetic at subtidal frequencies, there is significant energy in two diurnal peaks (O1 and K1) and two semidiurnal peaks (M2 and S2). K1 and M2 dominate, respectively, in their frequency band, and there are additional higher frequency harmonics of these tidal constituents that are most apparent in the Off Shore and Cross Shore VMs. At most tidal frequencies, the energy is enhanced at the surface and decays with depth.

In the surface currents, where spectral energy is enhanced, we examine the tidal component of the currents based on a 10% bandpass around the M2 and K1 frequencies, respectively, and a two-day highpass. Variance ellipses,[2] shown in Fig. 2(d)–(f), for each respective frequency band show that tidal contributions are highest in the Off Shore transect and lowest in the Along Shore transect. The eccentricity of each ellipse shows that tidal fluctuations are not strictly aligned with the vehicle path. In both the Off Shore and the Cross Shore transects, the M2 tide is more directional than the K1 tide, while in the Along Shore transect, both the tidal bands are directionally uncorrelated.

To understand the importance of tides with respect to the broader California Current System, Fig. 3 displays statistics of the amplitudes of bandpassed tidal components and the low-frequency component of the current, derived from a two-day lowpass. The amplitude of each tidal current is calculated with a 48-h windowed moving maximum, which is effectively measuring the envelope modulating the tidal currents. The amplitude of the lowpass signal is the absolute value of the along-track current component. Tidal amplitudes are strongest at the Off Shore VM and weakest at the Along Shore VM. This is opposite to the amplitude of the mean flow, which is clearly strongest at the Along Shore location. With respect to tidal amplitudes, both M2 and K1 components of the tides, individually, can be on the same order as the mean flow at the Off Shore and Cross Shore VM. This is not true at the Along Shore VM, where it is unlikely that the tides would dominate the mean flow.

D. Vertical Structure

Strong and/or persistent shear in the ocean currents would allow an AUV to increase efficiency by changing depth. Complex modal analysis (not shown) was performed on vertical profiles from each VM and showed that a significant amount of variance is explained by modes with a change in direction as a function of depth. We refer to mode zero as the mode that explains the most variance in the original data, which is characterized by a profile that is surface intensified and unidirectional. Mode zero accounts for between 80% and 83% of total variance for each transect. When including the next three to five modes, based on the specific transect, more than 95% of the total variance is explained. In these modes, there is a change in direction at depths less than approximately 200-m depth. Frequency analysis of the associated modal amplitudes shows that mode 0 is dominated by subtidal frequencies, while the higher order modes exhibit tidal peaks that are on the same order or exceed power in the low

[2]A variance ellipse is computed as an eigendecomposition of the covariance matrix between surface current components for a given time series [28]. The eigenvectors represent the principal components of the flow and therefore the orientation of the ellipse. The size of the ellipse is scaled to contain data within two standard deviations from the mean.

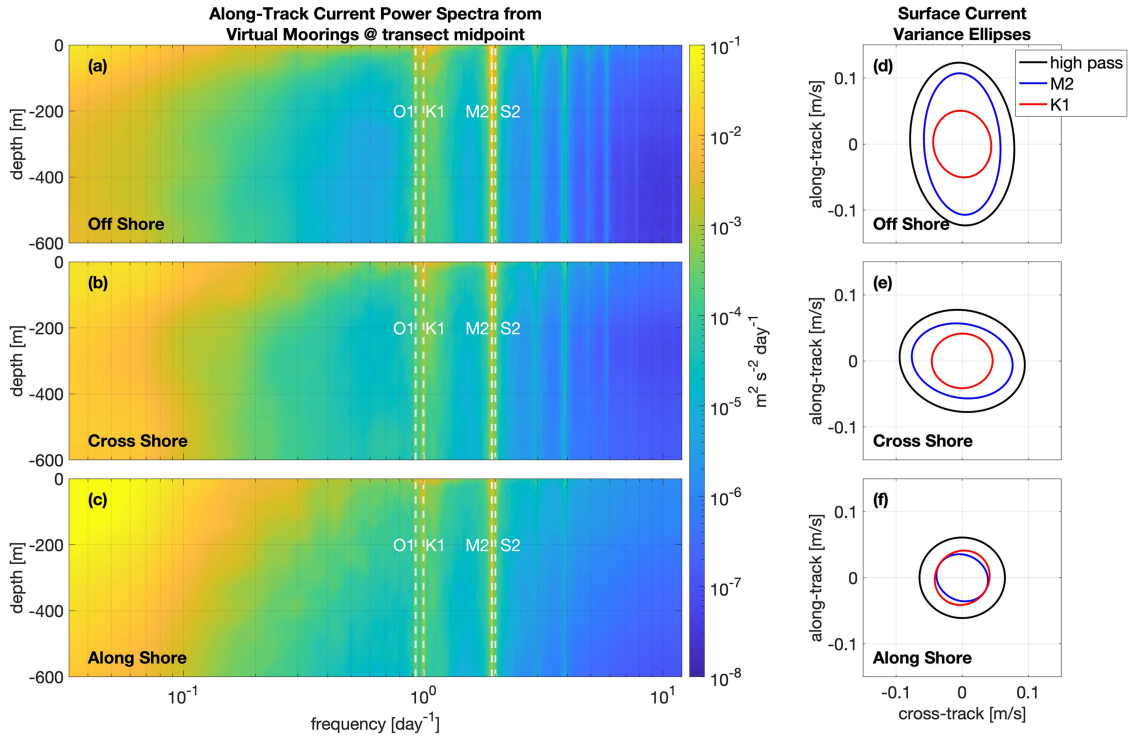

Fig. 2. Power spectra (a)–(c) of along-track currents at each VM as a function of depth and frequency. The dominant tidal frequencies for the region are annotated with white dashed lines and align well with peaks in power spectral density. Variance ellipses (d) and (e) are shown for surface currents at each VM. Separated with a two-day highpass (black), M2 bandpass (blue), and a K1 bandpass (red), the ellipse contours represent data within two standard deviations of the mean.

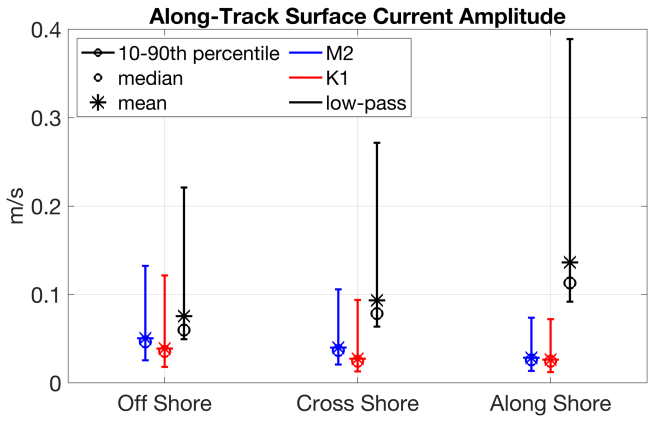

Fig. 3. Statistics of along-track, surface current amplitude for a 10% bandpass around M2 (blue), 10% bandpass around K1 (red), and two-day lowpass (black) computed over the entire two-year record and along each transect.

frequency. In addition, an analysis of temperature gradients at each VM shows that the mixed layer depth varies semiannually from approximately 100 m in winter to 25 m in summer. In the surface mixed layer, calculated using a change in temperature, there is greater variability in current velocities.

E. Along-Track Structure

If, over the course of a transit, flow is most intense at the surface and does not change direction, it would not be necessary to dynamically exploit vertical current shear. Instead, an intelligent choice of a constant operating depth would be sufficient for mission planning. To that end, we examine zero crossings of the along-track component of surface currents, where currents switch between aiding and impeding the AUVs' speed. Fig. 4 shows a Hovmöller diagram [29] for the along-track surface currents from the Off Shore transect, which highlights how the spatial features of surface currents evolve over time. Here, one can see that in a de-tided model [see Fig. 4(b)], there is one primary zero crossing that persists throughout the time shown. Qualitatively, a vehicle operating in this time window would benefit from avoiding strong head currents in the first 40–80 km of this mission, and then, it should ascend toward the surface in the second half of the mission to take advantage of strong tail currents. When including tidal forcing [see Fig. 4(a)], one can see that a more dynamic behavior is required. The tidal perturbations on the along-track current shift the main zero crossing forward or backward by up to 40 km and introduce new zero crossings where it would be advantageous to dive or climb. These changes occur on time scales that are either comparable to or shorter than the duration of a typical mission. In this scenario, manually determining the optimal control policy is not feasible, so we need an algorithmic solution.

Over the time range of the model, we compute the percentage of time steps, which have a given number of zero crossings for both the full and de-tided surface currents. The results are shown in Fig. 5. Notably, the Along Shore transect has the highest percentage of time steps without any zero crossings, and this percentage does not change much with the inclusion

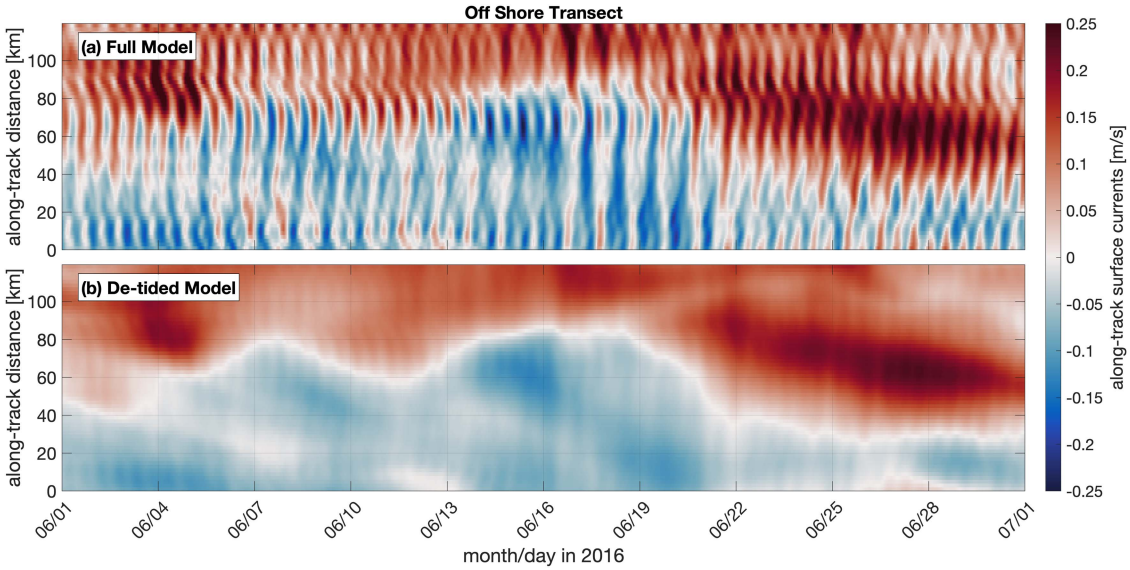

Fig. 4. Month-long Hovmöller diagram of along-track surface currents from the Off Shore transect. The original signal (a) shows semidiurnal perturbations to the underlying signal that can be attributed to the tidal components of the current. The de-tided signal (b) is calculated with a two-day running mean of the original signal. The inclusion of tidal currents can shift the along-track location of zero crossings of the current and in some cases introduce new crossings.

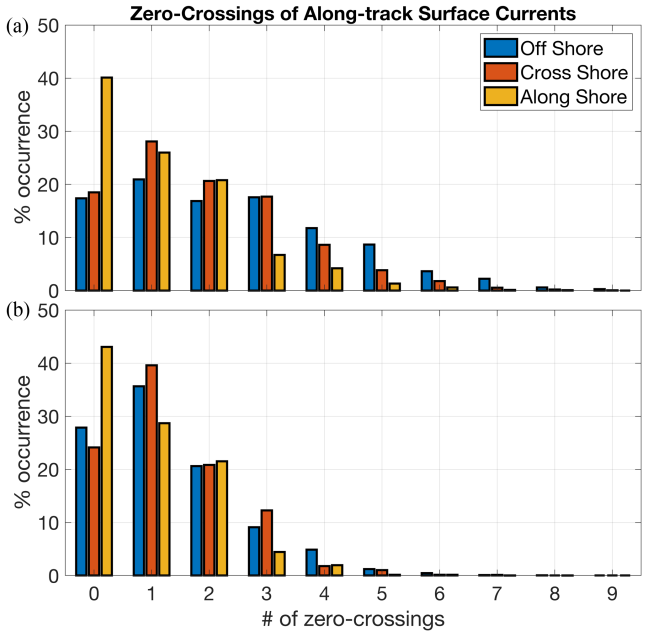

Fig. 5. Bar chart showing the percent occurrence of zero crossings in the along-track surface currents on each transect. Percent occurrence refers to the amount of hourly time steps from the entire record at which there are a specified number of zeros crossings in the along-track current as a function of distance. (a) Full model. (b) De-tided model.

of tides. This result is consistent with Fig. 3, which shows that the magnitude of along-track mean flow is significantly stronger than tidal fluctuations. For the other two transects where tidal amplitudes are often on the same order as the mean flow, the number of zero crossings increases significantly with the addition of tidal effects. For these transects, over 80% of model time steps contain one or more zero crossings.

III. Methods

A. Problem Statement

This study focuses on a medium-diameter AUV that navigates through a deterministic ocean current field that varies in 3-D and time. The AUV has control over its depth and speed, while it is constrained to a vertical plain following an obstacle-free shortest-distance path. Here, we focus on paths that do not collide with landmasses so that the vehicle will always travel along a great-circle arc, but, in general, existing techniques (e.g., visibility graph [30]) are available to compute suitable paths in cluttered environments. Under this constraint, path planning reduces to a 2-D time-varying problem. The AUV state vector $\mathbf{x} := (x, z, t)$ is defined by along-track distance x, depth z, and time t. We use the convention that $z = 0$ is the ocean surface and $z > 0$ is below the surface. A control input vector $\mathbf{u} := (n, \Delta z)$ is defined by its commanded propeller speed n and a *desired* change in depth Δz. After choosing the start and end points of the transect, the initial depth and launch time of the vehicle are explicitly defined. The vehicle is allowed to finish its transit at any depth. The cost of a given transit is quantified by the total energy consumed by the AUV.

B. Vehicle Simulation

The simulation considers vehicle motion and power consumption with respect to ocean currents and uses: 1) model output of ocean currents and bathymetry; 2) AUV speed over ground (SOG) and power models; 3) inverse kinematics for line-following in currents; and 4) a vehicle state motion model.

1) Flow Model: The simulation environment uses 3-D slices (along-track distance, depth, and time) of the ocean model characterized in Section II. Vertical velocities are assumed to be negligible and are ignored. Horizontal currents are linearly

TABLE II
VEHICLE MODEL PARAMETERS

Parameter Name	Symbol	Value
Advance Ratio	J	0.55
Propeller Diameter	d	0.3 m
Power Coefficient	C_p	0.08
Water Density	ρ	1025 kg m^{-3}
Hotel Load	P_h	100 W
Dive/Climb Pitch Angle	θ	20 °

interpolated to subgrid resolution to account for fine-scale vehicle motion. Due to the coarseness of the bathymetry in the model, we use a higher resolution bathymetric product (200 m) for seafloor avoidance [31]. Current values at the deepest grid point, defined using the high-resolution bathymetry product, are set to zero.

2) Vehicle Model: Vehicle dynamics and power consumption are modeled using the methods described in [24] that is based on an equilibrium force balance between vehicle thrust and hull drag resistance. In-water calibration experiments for a REMUS 600 determine the advance ratio J and the power coefficient C_p. These parameters as well other relevant constants are summarized in Table II. This model also provides expressions for through-water velocity $\mathbf{V}$ and power consumption P as a function of the control input.

The horizontal $V_x(\mathbf{u})$ and vertical $V_z(\mathbf{u})$ components of through water velocity are defined here

$$\begin{bmatrix} V_x(\mathbf{u}) & V_z(\mathbf{u}) \end{bmatrix} = \begin{cases} \Delta z = 0, & Jnd \begin{bmatrix} 1 & 0 \end{bmatrix} \\ \Delta z \neq 0, & Jnd \begin{bmatrix} \cos(\theta) & \frac{\Delta z}{|\Delta z|} \sin(\theta) \end{bmatrix} \end{cases} \tag{1}$$

as a function of the control input and vehicle parameters J, d, and θ that are summarized in Table II. The magnitude of the through-water velocity is proportional to the propeller speed. When $\Delta z = 0$, the velocity vector lies in the horizontal plane, and when $\Delta z \neq 0$, the velocity is divided between horizontal and vertical components based on a dive/climb angle θ, which is constant for all depth changes in a simulation. Diving or climbing are distinguished by a positive or negative sign of the control input Δz respectively.

Instantaneous power draw, $P(n)$, is a function of the commanded propeller speed and vehicle parameters from Table II: C_p, ρ, d, and P_h:

$$P(n) = C_p \rho n^3 d^5 + P_h. \tag{2}$$

We do not consider an additional power penalty for diving or climbing. The first term in (2) is the dynamic power draw that is proportional to the cube of the propeller speed. P_h is the constant hotel load (e.g., sensing, computing, and control).

3) Line Following: In addition to the input controls $\mathbf{u}$, we assume that the vehicle follows a line. This allows for a "crabbing" behavior, in which vehicle heading ψ deviates from the course over ground (COG) ϕ in the presence of local currents such that the vehicle maintains the prescribed course (a rudimentary navigation behavior found in most AUVs).

Following [1], we have

$$\psi(\mathbf{x}, \mathbf{u}, \phi) = \sin^{-1}\left(\frac{u_n(\mathbf{x}, \phi)}{V_x(\mathbf{u})}\right) + \phi. \tag{3}$$

Local currents u_ϕ and u_n are vector components rotated into a reference frame aligned with ϕ, resulting in the along-track and cross-track components of the current, respectively. In (3), we see that the vehicle heading deviates from ϕ such that a portion of V_x is used to offset the cross-track component of the current. As a direct result, one finds the equation for SOG $V_g(\mathbf{x}, \mathbf{u}, \phi)$ to be

$$V_g(\mathbf{x}, \mathbf{u}, \phi) = u_\phi(\mathbf{x}, \phi) + V_x(\mathbf{u}) \sqrt{1 - \left(\frac{u_n(\mathbf{x}, \phi)}{V_x(\mathbf{u})}\right)^2}. \tag{4}$$

The resulting SOG is a sum of the along-track component of the current and the remaining component of horizontal through-water velocity. Both (3) and (4) are subject to the constraint that the vehicle's horizontal speed through water exceeds the cross-track current magnitude $V_x > |u_n|$; otherwise, forward motion is not possible.

4) Motion Model: Vehicle movement is simulated based on the discrete motion model

$$\mathbf{x}' = f(\mathbf{x}, \mathbf{u}) = \mathbf{x} + \begin{bmatrix} \Delta x(\mathbf{x}, \mathbf{u}) \\ V_z(\mathbf{u}) \frac{\Delta x(\mathbf{x}, \mathbf{u})}{V_g(\mathbf{x}, \mathbf{u}, \phi)} \\ \frac{\Delta x(\mathbf{x}, \mathbf{u})}{V_g(\mathbf{x}, \mathbf{u}, \phi)} \end{bmatrix} \tag{5}$$

where control $\mathbf{u}$ is applied at the current state $\mathbf{x}$ resulting in a move to a new state $\mathbf{x}'$. The simulation step size Δx is defined by

$$\Delta x(\mathbf{x}, \mathbf{u}) = \min\left\{\Delta x_{\max}, \Delta x_\tau, \frac{V_g(\mathbf{x}, \mathbf{u}, \phi)}{V_z(\mathbf{u})} \Delta z\right\}. \tag{6}$$

The step size does not exceed $\Delta x_{\max} = 100$ m, which is chosen to meet stationary requirements over the course of a single step. Step size can be shortened at any point in the simulation if the distance to the terminal state Δx_τ or the horizontal distance necessary to complete its desired change in depth is less than $\Delta x_{\max}$. The energy consumed E by the vehicle for applying a control $\mathbf{u}$, from a state $\mathbf{x}$, is defined as

$$E(\mathbf{x}, \mathbf{u}) = \frac{P(n) \Delta x}{V_g(\mathbf{x}, \mathbf{u}, \phi)}. \tag{7}$$

C. Planning Algorithm

We propose a greedy algorithm [32] driven by the goal of real-time operation on an AUV using available sensors. Vehicle operating parameters that constrain the greedy algorithm are summarized in Table III.

The vehicle is assumed to have upward- and downward-facing ADCPs, which define the sensing range parameter Δz_{ADCP} (a realistic $\Delta z_{\text{ADCP}} = 10$ m is chosen to be consistent with a 1200-kHz ADCP). We assume a perfect sensor such that the environmental model can be directly queried within the sensing range from the vehicle, and we do not consider a model for sensor

TABLE III
VEHICLE OPERATING PARAMETERS

Parameter Name	Symbol	Value
Minimum Operating Depth	$z_{\min}$	5 m
Maximum Operating Depth	$z_{\max}$	600 m
Minimum Operating Altitude	a_0	10 m
ADCP Range	Δz_{ADCP}	10 m
Allowable Propeller Speeds	$\mathcal{N}$	[300, 600] rpm

uncertainty. We assume that the vehicle has onboard state estimation to allow for the measured currents to be rotated into the COG reference frame. In addition, the simulation includes a vehicle altimeter to sense distance from the bottom and to maintain a minimum altitude of a_0 above the seafloor. The set of allowable propeller speeds $\mathcal{N}$ is constrained between 300 and 600 rpm based on steerage and maximum operating speed, respectively. For this range of rpm, we find that the line-following constraint ($V_x > |u_n|$) can always be satisfied on a subset of allowable rpm. In strong cross currents, low propeller speeds that do not satisfy the line-following constraint are ignored during optimization.

Greedy decisions are based on the instantaneous rate of power consumption per unit distance dE/dx

$$\frac{dE}{dx}(\mathbf{x}, \mathbf{u}, \phi) = \frac{dE}{dt}\frac{dt}{dx} = \frac{P(n)}{V_g(\mathbf{x}, \mathbf{u}, \phi)}. \tag{8}$$

Minimization of dE/dx is computed over a joint control space of $\mathcal{N} \times \Delta\mathcal{Z}$. $\mathcal{N}$ is discretized over its specified range by steps of 5 rpm. $\Delta\mathcal{Z}$ is defined as the set of Δz to be considered at a given step in the algorithm. It depends on the depth of the vehicle z, the depth of the ocean at the vehicle location z_0, and the depth grid of the model $\mathbf{z}_{\text{grid}}$. Shown in (9), at the bottom of this page, $\Delta\mathcal{Z}$ is limited by ADCP sensing range, operating depths, and minimum altitude from the bottom. This construction is specific to simulation, as it only considers depths defined by the model grid. For an onboard implementation, $\Delta\mathcal{Z}$ can be defined at each depth that the currents are sensed by the ADCPs.

For a given step of the simulation, the vehicle is in state $\mathbf{x}$ with a COG to the terminal state of ϕ. To determine an optimal control input $\mathbf{u}^* = (n^{**}, \Delta z^*)$, we minimize dE/dx twice. First, we compute dE/dx as if the vehicle were operating at all $n \in \mathcal{N}$ with local currents interpolated at $(x, y, z') = (x, z + \Delta z, t) \forall \Delta z \in \Delta\mathcal{Z}$. The argument Δz^* from the pair $(n^*, \Delta z^*)$ that minimizes dE/dx is chosen as the desired change in depth. Next, the optimal propeller speed n^{**} is chosen by minimizing dE/dx where SOG is a function of the dive/climb angle necessary to achieve Δz^*, and the local currents are interpolated at $\mathbf{x}$. These optimizations are listed in (10) and (11). With a two-stage optimization, we have extended the algorithm previously studied in [24] to include optimization over the depth, which results in a dynamic depth-seeking behavior for the AUV

$$(n^*, \Delta z^*) = \underset{(n,\Delta z)\in\mathcal{N}\times\Delta\mathcal{Z}}{\arg\min} \frac{P(n)}{V_g((x, z + \Delta z, t), (n, 0), \phi)} \tag{10}$$

$$n^{**} = \underset{n\in\mathcal{N}}{\arg\min} \frac{P(n)}{V_g(\mathbf{x}, (n, \Delta z^*), \phi)}. \tag{11}$$

The optimal control is applied to update the vehicle's state $\mathbf{x}' = f(\mathbf{x}, \mathbf{u}^*)$, with the associated energy cost $E(\mathbf{x}, \mathbf{u}^*)$. This behavior is iterated from the initial condition until the vehicle has reached the endpoint. Total energy expenditure is calculated as the sum of energy consumed across the transit.

The energy consumption of a vehicle with the parameters outlined above is chosen to have a realistic ADCP sensor range and is labeled "±10 m sensing." We also consider two different vehicle configurations: 1) "full-depth sensing" denotes a vehicle with ADCP range $\Delta z_{\text{ADCP}} = 600$ m in which the vehicle has full information of the current profile at its local position and time (It should be noted that the authors classify this behavior as "onboard" since the vehicle lacks the ability to anticipate the currents it will encounter along its future journey.); and 2) "constant depth" denotes a vehicle with $\Delta z_{\text{ADCP}} = 0$ m, which only optimizes n. Transiting at a fixed depth is standard practice, and the adaptive choice of propeller speed was studied in [24]. When operating at constant depth, a basic seabed obstacle avoidance behavior allows the AUV to maintain an altitude of a_0 when obstructed. Fig. 6(a)–(c) demonstrates the difference between these configurations for one example simulation.

IV. RESULTS

Results are presented for simulations spanning a two-year window with hourly initializations at multiple initial depths. The Off Shore and Cross Shore transects are initialized at $z_{\text{init}} = \{5, 50, 100, 200, 300, 400, 500, 595\}$ m. The Along Shore transect is initialized at the same depths excluding 500 and 595 m, due to bathymetry constraints. In practice, all vehicles start at the surface and are driven down to the prescribed depth. We do not consider the initial dive's contribution to total energy consumption because it is negligible relative to the energy consumed over the total transit.

The equations of motion and the energy saving behavior are implemented in MATLAB using the simulation framework outlined in [33]. Simulations were run on a Dell Laptop running Ubuntu with a six-core Intel Core i7 Processor at 2.70 GHz with 64 GB of RAM. Runs within each ensemble were simulated in

$$\begin{aligned}
\Delta\mathcal{Z}(z, z_0) &:= \{0, \Delta z_{\max,\text{climb}}, \Delta z_{\max\,\text{dive}}, \Delta\mathcal{Z}_{\text{grid}}\} \\
\textbf{s.t.}\quad \Delta z_{\max,\text{climb}} &= \min(-\Delta z_{\text{ADCP}}, z_{\min} - z) \\
\Delta z_{\max\,\text{dive}} &= \max(\Delta z_{\text{ADCP}}, \max(z_{\max}, z_0 + a_0) - z) \\
\Delta\mathcal{Z}_{\text{grid}} &:= \{\Delta z = z' - z, z' \in \mathbf{z}_{\text{grid}} \mid \Delta z_{\max,\text{climb}} < \Delta z < \Delta z_{\max,\text{dive}}\}.
\end{aligned} \tag{9}$$

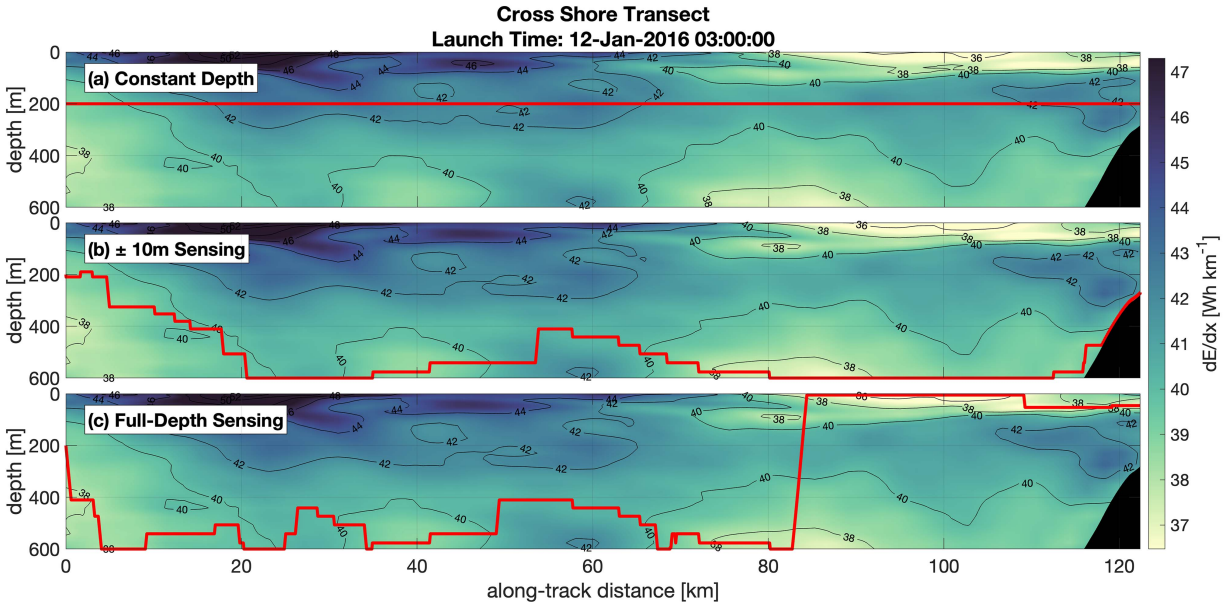

Fig. 6. Example vehicle tracks (red) from a single simulation of the Cross Shore transect for each vehicle configuration. Values of dE/dx are contoured for all depths that the vehicle could transit. Each vehicle configuration starts at the same time and initial depth of 200 m. The climb taken by the vehicle in (c) at 80 km highlights benefit of full-depth sensing, where the realistic sensor (b) is not able to find the low dE/dx region at the surface once already at depth.

TABLE IV
TRANSIT TIME MEAN AND STANDARD DEVIATION FOR ALL SIMULATIONS FOR EACH TRANSIT AND BEHAVIOR

	Off Shore	Cross Shore	Along Shore
Constant Depth	31.7 ± 0.7 h	32.9 ± 0.9 h	27.8 ± 1.5 h
±10 m Sensing	31.0 ± 0.8 h	32.2 ± 1.0 h	26.9 ± 1.3 h
Full-Depth Sensing	30.7 ± 0.8 h	31.8 ± 0.9 h	26.8 ± 1.4 h

parallel using the MATLAB parallel computing toolbox. The runtime of a single simulation was approximately 0.13 s.

Although our greedy algorithm does not guarantee transit completion, for this set of simulations, there are no failures from strong currents. The only failures occur for simulations that are initialized at the very end of the model time window and thus do not complete the transit before 1 January 2018. This results in between 17 510 and 17 515 individual simulations for each transit and initial depth pair. Each statistical distribution is calculated over this dimension, indexed by launch time.

While each sensing configuration affects the transit time for a given simulation, the focus of our analysis is energy consumption. For completeness, Table IV summarizes the average transit time, across initial depth conditions, for the full ensemble of simulation start times, for each transect and configuration. The duration of each transit is between 1 and 1.5 days. Tidal variations occur on the same time scale, underscoring their important role in optimizing the vehicle's route.

A. Energy Consumption

Fig. 7 summarizes energy consumption, normalized by transect length, for all simulations. The distributions for constant depth, shown in Fig. 7(a)–(c), and ±10 m sensing, shown in Fig. 7(d)–(f), change as a function of the initial depth and transect. However, the shaded distribution, from a vehicle with full-depth sensing, does not depend on z_{init}. When sensing the full water column, all initial conditions quickly converge to the same depth, and there is no significant difference in the resulting energy consumption.

In the distributions of energy consumption from simulations at constant depth, there is high variability at shallow initial depths and a narrow peak at deep initial depths. This trend can be attributed to enhanced current velocities at the surface and is most apparent in the Off Shore transit. The Along Shore transit distribution has the highest spread in the vehicle operating closest to the surface, but the distributions for deep initial conditions do not narrow as much as the other two transects.

With the ±10 m sensing range, shown in Fig. 7(d)–(f), the sets of distributions for each transect converge toward the shaded full-sensing distribution. The variability that remains between the distributions for a specific transect arises from the greedy approach of the algorithm. In the Off Shore and Cross Shore transits, each distribution skews toward lower energy consumption when launching closer to the ocean surface. But when launching at depths shallower than 100 m, this trend in the right tail of the distribution reverses and the probability of high energy consumption increases. The Along-Shore distributions do not reveal these same trends and, for the most part, converge to the same distribution as a vehicle with full-depth sensing.

To evaluate how much energy can be saved by using the adaptive behavior, we compare the energy consumption between ±10 m sensing and constant depth operation when launched at the same initial depth. The distributions of relative energy consumption, shown in Fig. 8, are normalized by the energy consumed using the constant depth behavior. For each transect,

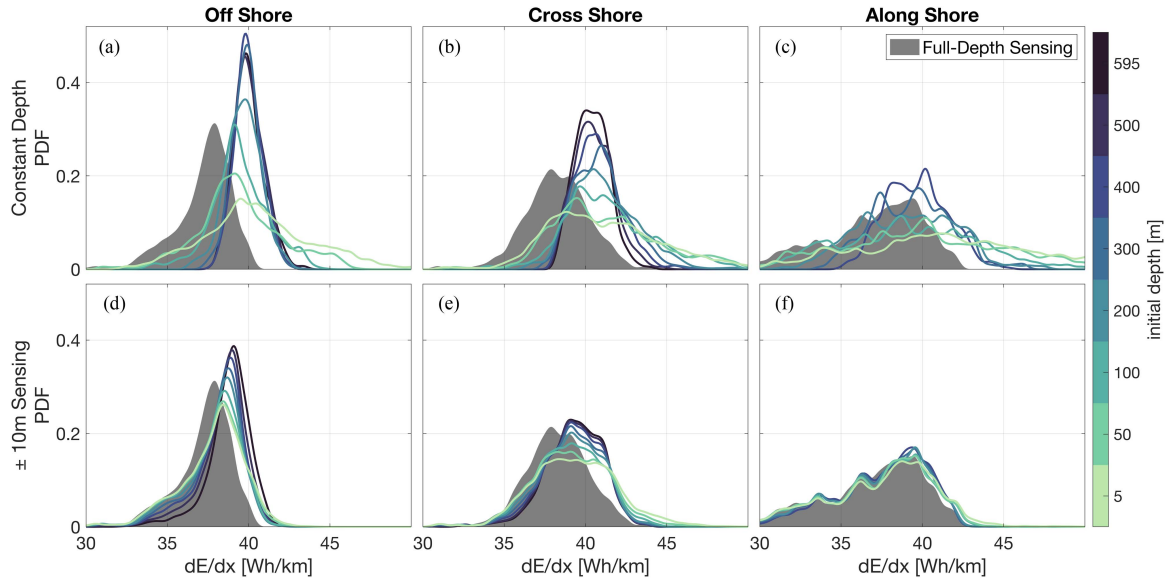

Fig. 7. Summary of results for two years of simulations on three transects. PDFs of energy consumption normalized by transect length are shown for a vehicle simulated with (a)–(c) constant depth and (d)–(f) the ±10 m sensing behavior. Each distribution is colored by its initial depth. The shaded PDFs in both rows represent results for the full-depth sensing behavior.

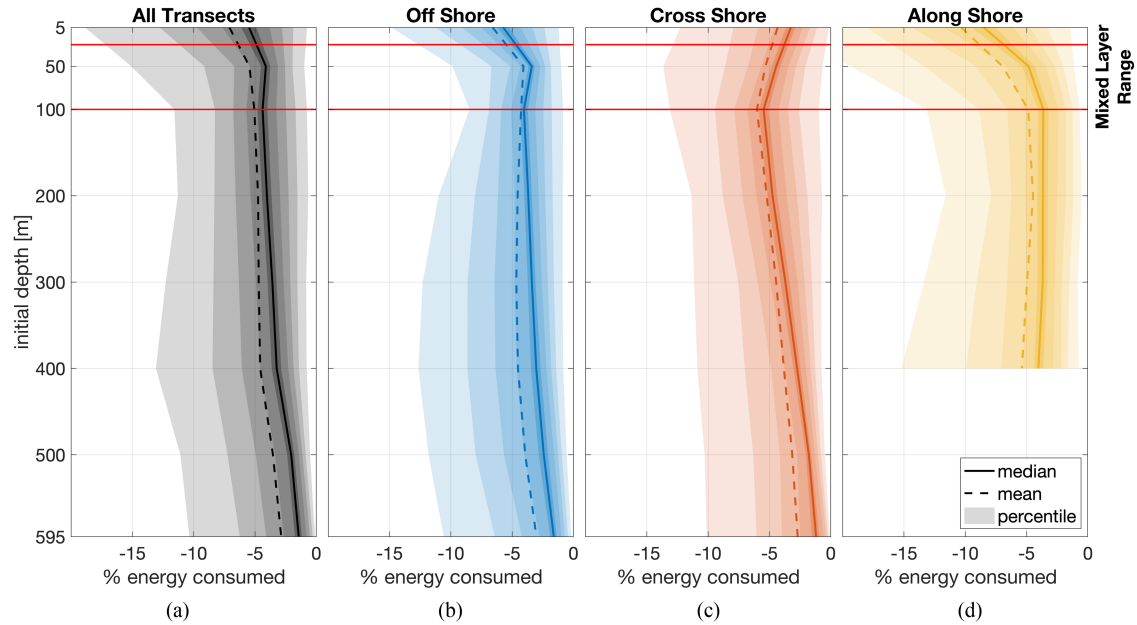

Fig. 8. Comparison of energy consumed when operating with the ±10 m sensing behavior referenced to constant depth simulations with common initial conditions. For each initial condition, the median (solid), mean (dashed), and 10% interval percentiles from 5% to 95% (contours) are shown. Red lines annotate the range of the mixed layer from summer to winter. Subplot (a) is an aggregate of all simulated transects, while subplots (b)–(d) represent individual transects.

more than 95% of simulation runs predict energy savings when using the greedy behavior. On average, energy savings range from 6% in comparing shallow initial depths to 3% at the deepest initial depth. The most extreme instances of energy savings come from the Along Shore transect [see Fig. 8(d)], where in certain conditions, launching close to the surface can lead to energy savings that exceed 20%. Across the different transects, the distributions are similar for deep initial depths, but each transect has a different distribution when launched at and above 100-m depth. This division is consistent with the base of the seasonal mixed layer.

B. *Initial Depth Sensitivity*

In most scenarios, the starting position and launch time of the vehicle are dictated by a given mission, while the initial depth is open to further optimization. To examine the effects of initial depth, consider "% Energy Anomaly" as $(\mathbf{c}_t - \langle \mathbf{c}_t \rangle)/\langle \mathbf{c}_t \rangle \cdot 100$,

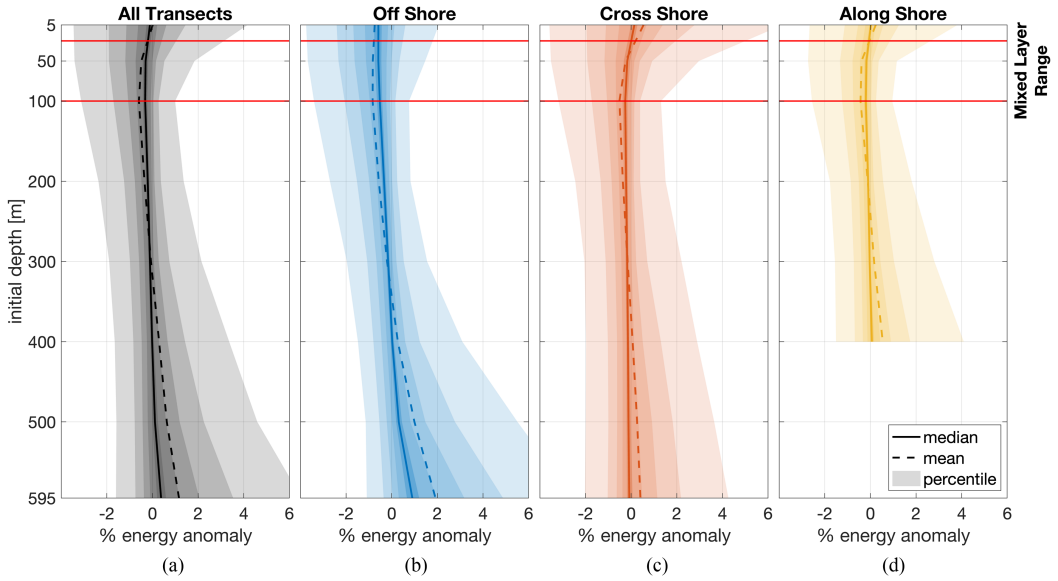

Fig. 9. Distributions of percent energy anomaly with respect to the average energy consumption across initial depth conditions, with statistics calculated over two years of simulation. For each initial condition, the median (solid), mean (dashed), and 10% interval percentiles from 5% and 95% (contours) are shown. Red lines annotate the range of the mixed layer from summer to winter. Subplot (a) is an aggregate of all simulated transects, while subplots (b)–(d) represent individual transects.

where $\mathbf{c}_t$ is the vector of total energy consumption for simulations at each initial depth at the same launch time, and the $\langle\cdot\rangle$ operator computes the mean. The distributions of this metric are summarized in Fig. 9. When ascending from a 595- to a 100-m initial depth, these distributions shift toward energy savings (right to left). Above 100 m, the distribution spreads out in both directions. Therefore, one can interpret the "safest" initial condition to be 100 m, where there is a minimum in both the expected energy anomaly and in the 95th percentile contour. This minimum is consistent with the base of the seasonal mixed layer, where one expects the strongest gradient in currents.

C. Tidal Effects on Vehicle Path

Until now, we have focused on the total energy consumption of each behavior. To analyze the depth choices of each vehicle that occur within a single simulation, we use empirical orthogonal functions (EOFs) [34], [35], [36]. Let $\mathbf{D} \in \mathbb{R}^{M\times N}$ be a matrix of vehicle depth anomaly. Anomaly is defined as the deviation from the time-averaged vehicle depth at each step in along-track distance. There are M rows indexed by the along-track distance (spatial points), and N columns indexed by the start time of a particular simulation (temporal points). We refer to a column of this matrix as the "depth profile" of the vehicle. Since (6) allows for variable distance discretization between simulation steps, vehicle depth profiles are interpolated onto a regular grid in along-track distance with a resolution of 50 m.

Numerically, it was shown in [37] that an EOF decomposition can be accomplished efficiently using the singular value decomposition, as defined in the following equation:

$$\mathbf{D} = \mathbf{U}\mathbf{\Sigma}\mathbf{V}^T \tag{12}$$

where the columns of $\mathbf{U} \in \mathbb{R}^{M\times M}$ and $\mathbf{V} \in \mathbb{R}^{N\times N}$ provide an orthonormal basis set of $\mathbf{D}$ that are uncorrelated in space and time, respectively. When $M < N$, $\mathbf{\Sigma} \in \mathbb{R}^{M\times N}$ has an upper $M \times M$ diagonal matrix of singular values, with s_m corresponding to each mode m. We use the terminology that the columns of $\mathbf{U}$ define the "modes" of our data, which are scaled at each time step by the "amplitudes" $\mathbf{A} = \mathbf{\Sigma}\mathbf{V}^T$. With respect to the original data set, $\mathbf{D}$, the percent of variance explained by mode is defined by $s_m^2/(\sum_{m=1}^{M} s_m^2)$.

Fig. 10 summarizes the results of an EOF analysis for simulations of the Off Shore transect with an initial depth of 5 m. The top five modes, explaining approximately 95% of total variance, each demonstrate a dive/climbing deviation from the average profile with decreasing length scales. In their frequency response, we see that each mode oscillates with a diurnal and semidiurnal frequency and a notably distinct peak at the M2 tidal frequency.

The same analysis was completed for each ensemble of simulations with a different initial condition (not shown), and the resulting mode shapes are shown in Fig. 11(b)–(f). Despite the different initial conditions, the mode shapes exhibit nearly identical behavior in terms of dive/climb length scales. Each shape also sorts in the same order based on the explained variance. This finding suggests that the scales at which the vehicle needs to adjust its depth are not significantly affected by its initial condition. While mode shapes are similar, Fig. 11(a) shows that the average depth of the AUV is biased based on the initial condition. Therefore, in physical space, variable initial conditions will lead to different depth profiles with variability in total energy consumption.

EOF analysis was also completed for vehicle simulations with full-depth sensing. Fig. 12 summarizes the same analysis as

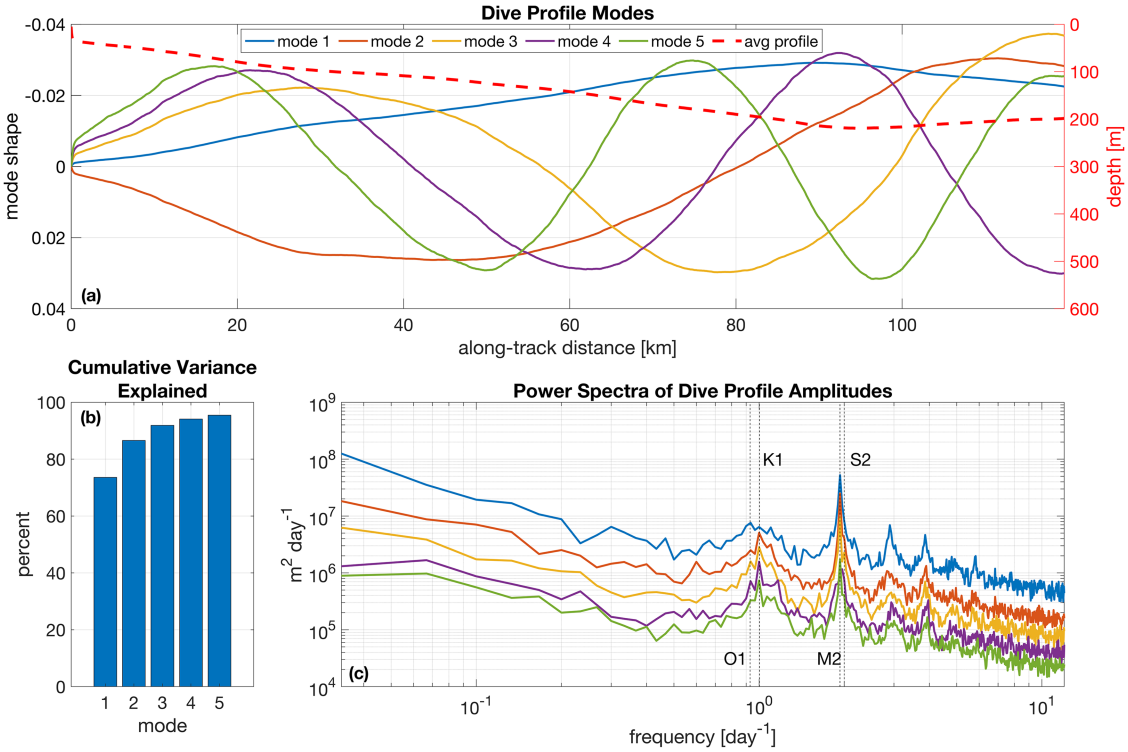

Fig. 10. Summary of EOF analysis for simulations of the Off Shore Transect with an initial depth of 5 m and a ±10 m sensing capability. Mode shape (a) and the power spectra of mode amplitudes (c) are shown for the first five most significant modes, explaining approximately 95% of the total variance in vehicle depth profiles (b). Variance is computed relative to the average depth profile [red dashed line in panel (a)] from all simulations with the specified initial depth and sensing capability.

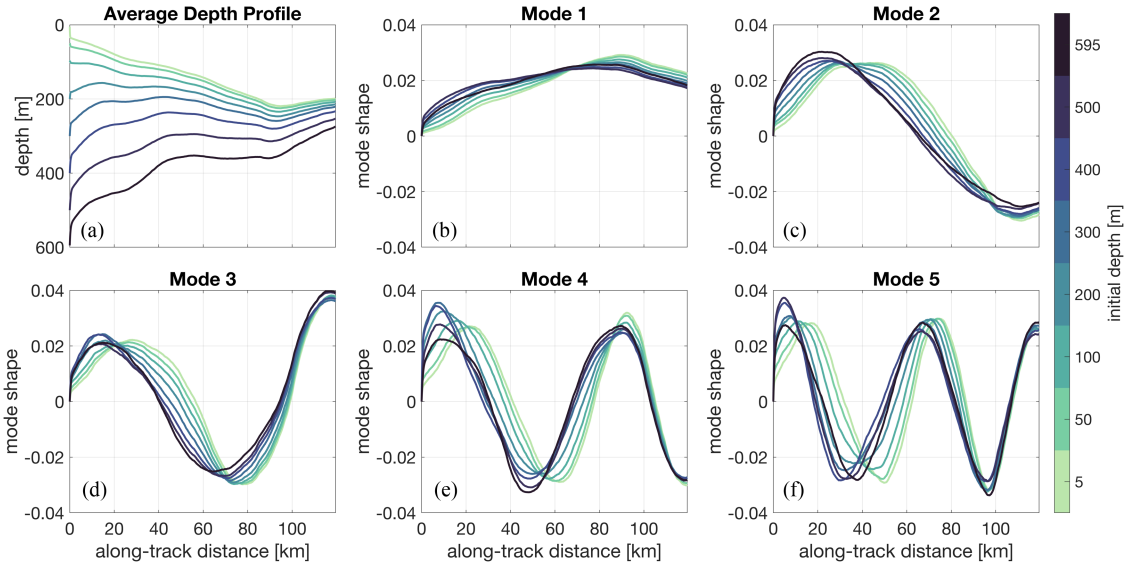

Fig. 11. Top five mode shapes in order of explained variance (b)–(f) and the average depth profile (a) as a function of along-track distance. Each line is colored by the initial depth condition for that set of simulated transits.

above, but it is notable that the first five modes of this decomposition explain significantly less of the total variance. With enhanced sensing capabilities, the AUV can respond to minor gradients, leading it to make more complex control decisions that cannot be captured with just a few modes. This is highlighted by the mode shapes in Fig. 12(a), which are much more complicated than those in Fig. 11(a). One can see that the modes are much more closely tied to the relevant tidal constants. In comparing the power spectrum in Fig. 12(c) to that in Fig. 10(c), the former has defined peaks that align with all four major tidal

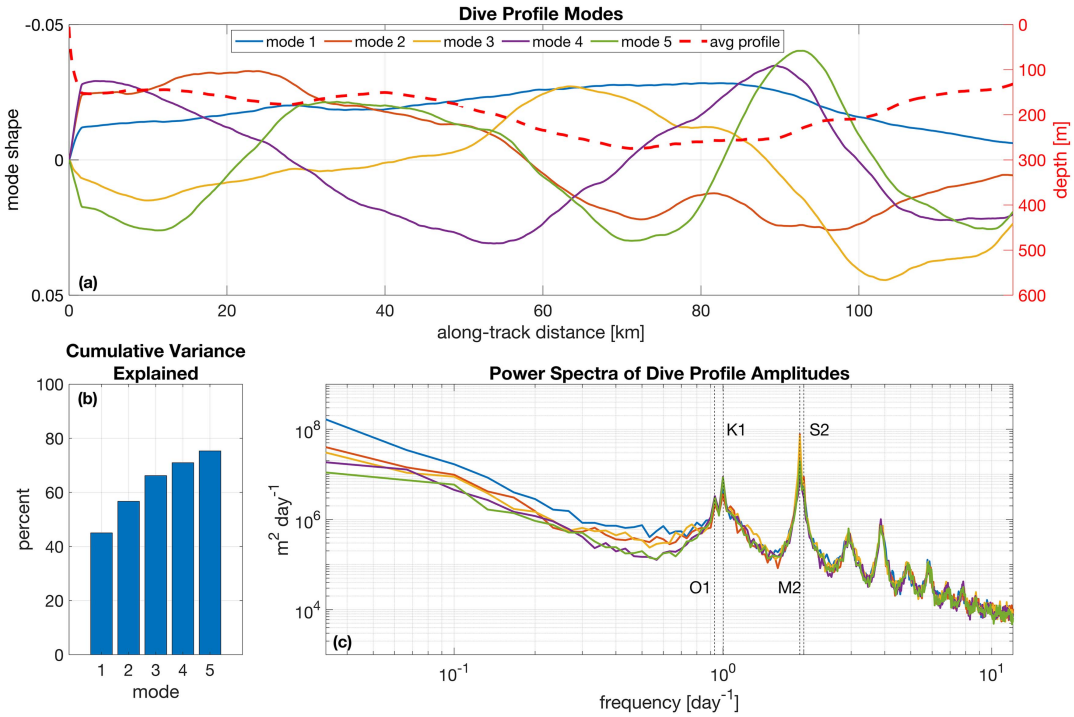

Fig. 12. Summary of EOF analysis for simulations of the Off Shore Transect with an initial depth of 5 m and full-depth sensing. Mode shape (a) and the power spectra of mode amplitudes (c) are shown for the first five most significant modes, explaining approximately 75% of the total variance in vehicle depth profiles (b). Variance is computed relative to the average depth profile [red dashed line in panel (a)] from all simulations with the specified initial depth and sensing capability.

constituents. The latter does resolve the M2 peak well, but the diurnal peak does not have a clear separation between the K1 and O1 frequencies.

V. Discussion and Conclusion

Considering sensing and computational capabilities onboard an AUV, we develop a new greedy behavior for energy-efficient path planning. We limit the vehicle to follow predefined paths of shortest distance over ground and focus on dynamically optimizing its depth and speed. A high-resolution tidally resolving ocean model is used to represent the vehicle's operating environment. An analysis in the Southern California Bight reveals the potential for significant energy savings by exploiting ocean current variability as a function of depth. Our behavior is compared to operating at a fixed depth by studying the distribution of energy savings along three transects chosen to represent regional ocean variability. Energy savings between 3% and 10% are typical, depending on the initial depth. Maximum energy savings are achieved when comparing vehicles initialized at the surface of the ocean, which, under certain conditions, can exceed 20%. These savings are applicable to missions with an extended transit into an operational area, at which point additional energy enables more time on station or increased data collection. Additional energy savings are also beneficial for mapping and sampling larger scale features that require long-term deployments.

For an AUV using the behavior with a sensing range of ± 10 m, we analyze the variability in energy consumption as a function of the initial depth. On average, we find that an initial depth of approximately 100 m appears to be optimal, which matches the depth of the surface mixed layer from the environmental model. It is reasonable to suppose that initializing at the base of the mixed layer is preferable due to the proximity to high gradients in along-track currents. Given the AUV's limited view of the water column, it is less likely to get caught in local features at the extreme ends of its operating depths.

The greedy algorithm is computationally efficient relative to global methods, which allows us to rapidly vary location, initial conditions, and parameters that represent variable sensing capabilities. Our results derived from densely observed statistical distributions, rather than a limited number of runs, provide a broader perspective on potential energy savings. While there is minimal seasonality in the Southern California Bight, our method would be useful for studying seasonal variations in energy savings in different operating environments. The large ensemble of simulation runs made it possible to explore data-driven techniques, namely, EOFs, to analyze the structure of the optimal solutions. This analysis showed that the depth profiles, adaptively chosen by the algorithm during a simulation, can be simplified into lower dimensional representations using a few common modes. The fact that these modes oscillate with predictable tidal frequencies encourages future work to design algorithms for optimal planning based on tides without the need for full domain knowledge.

Our results show that the greedy algorithm can outperform an AUV operating at constant depth, but it is still desirable to understand how close the algorithm is to approaching the lower bound set by a globally optimal solution. A comparison with

existing methods for the same number of simulation iterations is not computationally feasible. Future work could continue in the classical sense of improving and extending algorithms for greater numerical efficiency. Or it could focus on improved sampling schemes of environmental and path realizations such that the same energy consumption distributions could be represented with fewer samples, allowing for a more computationally costly optimization methods. A comparison to globally optimal solutions may highlight how this behavior is limited in environments where the horizontal shear in ocean currents dominates over vertical shear. In this case, the algorithms presented in [1] or [23] may be more advantageous.

Ultimately, in-water testing is crucial for the adoption of this algorithm. The vehicle model and the cost function introduced here, while idealized, are tailored to real-world vehicle and sensing constraints. Future efforts will focus on integrating this algorithm into a REMUS AUV using the backseat control protocol developed in [38]. When implementing on an AUV, it is essential to assess the accuracy of ocean current measurements by considering sensor noise and uncertainty in the AUV's own state estimation. In addition, the presence of errors in assumed vehicle geometry, sensor alignment, and calibration coefficients may pose challenges in accurately computing dE/dx and determining optimal control inputs. Once validated, we hope that this behavior will be used to extend AUV deployments and increase data collection for scientific process studies.

Acknowledgment

The authors would like to thank four anonymous reviewers for their time and effort in improving this manuscript. The authors would also like to thank the Office of Naval Research for their enduring support for undersea research.

References

[1] R. E. Davis, N. E. Leonard, and D. M. Fratantoni, "Routing strategies for underwater gliders," *Deep Sea Res. II, Topical Stud. Oceanogr.*, vol. 56, no. 3, pp. 173–187, Feb. 2009.

[2] M. Panda, B. Das, B. Subudhi, and B. B. Pati, "A comprehensive review of path planning algorithms for autonomous underwater vehicles," *Int. J. Autom. Comput.*, vol. 17, no. 3, pp. 321–352, 2020, doi: 10.1007/s11633-019-1204-9.

[3] B. Garau, A. Alvarez, and G. Oliver, "Path planning of autonomous underwater vehicles in current fields with complex spatial variability: An A* approach," in *Proc. IEEE Int. Conf. Robot. Autom.*, Apr. 2005, pp. 194–198.

[4] D. Rao and S. B. Williams, "Large-scale path planning for underwater gliders in ocean currents," in *Proc. Australas. Conf. Robot. Autom.*, 2009.

[5] D. Kularatne, S. Bhattacharya, and M. Ani Hsieh, "Time and energy optimal path planning in general flows," in *Proc. Robot.: Sci. Syst. Conf.*, 2016.

[6] D. Kularatne, S. Bhattacharya, and M. Hsieh, "Going with the flow: A graph based approach to optimal path planning in general flows," *Auton. Robots*, vol. 42, pp. 1369–1387, 2018.

[7] T. Lolla, M. P. Ueckermann, K. Yigit, P. J. Haley, and P. F. J. Lermusiaux, "Path planning in time dependent flow fields using level set methods," in *Proc. IEEE Int. Conf. Robot. Autom.*,, 2012, pp. 166–173.

[8] C. S. Kulkarni and P. F. J. Lermusiaux, "Three-dimensional time-optimal path planning in the ocean," *Ocean Model.*, vol. 152, 2020, Art. no. 101644.

[9] I. Hoteit, B. Cornuelle, S. Y. Kim, G. Forget, A. Köhl, and E. Terrill, "Assessing 4D-VAR for dynamical mapping of coastal high-frequency radar in San Diego," *Dyn. Atmos. Oceans*, vol. 48, no. 1, pp. 175–197, 2009.

[10] E. W. Dijkstra, "A note on two problems in connexion with graphs," *Numer. Math.*, vol. 1, no. 1, pp. 269–271, 1959.

[11] P. E. Hart, N. J. Nilsson, and B. Raphael, "A formal basis for the heuristic determination of minimum cost paths," *IEEE Trans. Syst. Sci. Cybern.*, vol. SSC-4, no. 2, pp. 100–107, Jul. 1968.

[12] S. LaValle, "Rapidly-exploring random trees: A new tool for path planning," Dept. Comput. Sci., Iowa State Univ., Ames, IA, USA, Tech. Rep. 9811-1998, 1998.

[13] D. N. Subramani, T. Lolla, P. J. Haley, and P. F. J. Lermusiaux, "A stochastic optimization method for energy-based path planning," in *Dynamic Data-Driven Environmental Systems Science* (Lecture Notes in Computer Science Series),S. Ravela and A. Sandu, Eds. Cham, Switzerland: Springer, 2015, pp. 347–358.

[14] M. M. Doshi, M. S. Bhabra, and P. F. J. Lermusiaux, "Energy–time optimal path planning in dynamic flows: Theory and schemes," *Comput. Methods Appl. Mech. Eng.*, vol. 405, Feb. 2023, Art. no. 115865.

[15] J. J. Heon Lee, C. Yoo, S. Anstee, and R. Fitch, "Hierarchical planning in time-dependent flow fields for marine robots," in *Proc. IEEE Int. Conf. Robot. Autom.*, May 2020, pp. 885–891.

[16] C. Cheng, Q. Sha, B. He, and G. Li, "Path planning and obstacle avoidance for AUV: A review," *Ocean Eng.*, vol. 235, Sep. 2021, Art. no. 109355.

[17] D. Fu-Guang, J. Peng, B. Xin-Qian, and W. Hong-Jian, "AUV local path planning based on virtual potential field," in *Proc. IEEE Int. Conf. Mechatronics Autom.*, 2005, pp. 1711–1716.

[18] O. Khatib, "Real-time obstacle avoidance for manipulators and mobile robots," in *Proc. IEEE Int. Conf. Robot. Autom.*, Mar. 1985, vol. 2, pp. 500–505.

[19] J. Yang, J. Ni, M. Xi, J. Wen, and Y. Li, "Intelligent path planning of underwater robot based on reinforcement learning," *IEEE Trans. Autom. Sci. Eng.*, vol. 20, no. 3, pp. 1983–1996, Jul. 2023.

[20] A. Guerrero-González, F. García-Córdova, and J. Gilabert, "A biologically inspired neural network for navigation with obstacle avoidance in autonomous underwater and surface vehicles," in *Proc. IEEE OCEANS Conf.*, Jun. 2011, pp. 1–8.

[21] B. Cole, M. R. Benjamin, and S. Randeni, "AIS-based collision avoidance in MOOS-IvP using a geodetic unscented Kalman filter," in *Proc. IEEE OCEANS Conf.*, Sep. 2021, pp. 1–10.

[22] M. R. Benjamin, M. Defilippo, P. Robinette, and M. Novitzky, "Obstacle avoidance using multiobjective optimization and a dynamic obstacle manager," *IEEE J. Ocean. Eng.*, vol. 44, no. 2, pp. 331–342, Apr. 2019.

[23] B. Garau, A. Alvarez, and G. Oliver, "AUV navigation through turbulent ocean environments supported by onboard H-ADCP," in *Proc. IEEE Int. Conf. Robot. Autom.*, May 2006, pp. 3556–3561.

[24] J. Chang et al., "Power efficiency autonomy for long duration AUV operation," in *Proc. IEEE/OES Auton. Underwater Veh. Symp.*, Sep. 2022, pp. 1–6.

[25] R. Stokey et al., "Development of the REMUS 600 autonomous underwater vehicle," in *Proc. MTS/IEEE OCEANS Conf.*, Sep. 2005, pp. 1301–1304.

[26] M. R. Mazloff, B. Cornuelle, S. T. Gille, and J. Wang, "The importance of remote forcing for regional modeling of internal waves," *J. Geophys. Res.: Oceans*, vol. 125, no. 2, Feb. 2020, Art. no. e2019JC015623.

[27] P. Welch, "The use of fast Fourier transform for the estimation of power spectra: A method based on time averaging over short, modified periodograms," *IEEE Trans. Audio Electroacoust.*, vol. 15, no. 2, pp. 70–73, Jun. 1967.

[28] R. E. Thomson and W. J. Emery, "Statistical methods and error handling," in *Data Anal. Methods in Phys. Oceanogr.*, 3rd ed., R. E. Thomson and W. J. Emery, Eds., Boston, MA, USA: Elsevier, Jan. 2014, ch. 3, pp. 219–311.

[29] E. Hovmöller, "The trough-and-ridge diagram," *Tellus*, vol. 1,no. 2, pp. 62–66, 1949.

[30] H. Niu, A. Savvaris, A. Tsourdos, and Z. Ji, "Voronoi-visibility roadmap-based path planning algorithm for unmanned surface vehicles," *J. Navigat.*, vol. 72, no. 4, pp. 850–874, Jul. 2019.

[31] California Department of Fish and Wildlife, "Bathymetric digital elevation model (200 meters): California coast, 2002," *Mar. Region GIS Lab*, 2003. [Online]. Available: http://purl.stanford.edu/ns150wp8904

[32] T. H. Cormen, C. E. Leiserson, and R. L. Rivest, *Introduction to Algorithms*. Cambridge, MA, USA: MIT Press, Jun. 1990.

[33] R. Young, S. Merrifield, M. Anderson, and E. Terrill, "A simulation framework for environmentally-aware autonomous underwater vehicle (AUV) mission planning and algorithm development," in *Proc. MTS/IEEE OCEANS Conf.*, Sep. 2023, pp. 1–6.

[34] R. Preisendorfer and C. Mobley, *Principal Component Analysis in Meteorology and Oceanography*, C. D. Mobley, Ed., New York, NY, USA:Elsevier, 1988.

[35] E. N. Lorenz, "Empirical orthogonal functions and statistical weather prediction," Dept. Meteorol., Massachusetts Inst. Technol., Cambridge, MA, USA, Sci. Rep. 1, 1956.
[36] R. E. Davis, "Predictability of sea surface temperature and sea level pressure anomalies over the north pacific ocean," *J. Phys. Oceanogr.*, vol. 6, no. 3, pp. 249–266, May 1976.
[37] K. A. Kelly, "Comment on 'Empirical orthogonal function analysis of advanced very high resolution radiometer surface temperature patterns in Santa Barbara Channel' by G. S. E. Lagerloef and R. L. Bernstein," *J. Geophys. Res.: Oceans*, vol. 93, no. C12, pp. 15753–15754, 1988.
[38] E. Gallimore, R. Stokey, and E. Terrill, "Robot operating system (ROS) on the REMUS AUV using RECON," in *Proc. IEEE/OES Auton. Underwater Veh. Workshop*, 2018, pp. 1–6.

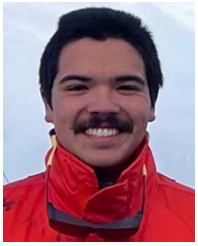

Raymond Young received the B.S. and M.S. degrees in mechanical engineering from the University of California San Diego, San Diego, CA, USA, in 2020 and 2022, respectively, where he is currently working toward the Ph.D. degree with the Scripps Institution of Oceanography.

He is also a National Defense Science and Engineering Graduate Fellow studying Oceanography (Applied Ocean Science) with the Scripps Institution of Oceanography, University of California San Diego. His research interests include autonomous marine vehicles, optimal control, and robotic path planning.

Sophia Merrifield received the Ph.D. degree in physical oceanography from the Massachusetts Institute of Technology/Woods Hole Oceanographic Institution Joint Program, Cambridge, MA, USA, in 2016.

She is currently an Associate Researcher with the Scripps Institution of Oceanography, University of California San Diego, San Diego, CA, USA. Her research interests include marine vehicle autonomy and oceanic turbulence.

Mark Anderson received the Ph.D. degree in aeronautical and astronautical engineering from Purdue University, West Lafayette, IN, USA, in 1988.

Previously, he held a faculty position with the Department of Aerospace and Ocean Engineering, Virginia Polytechnic Institute and State University, Blacksburg, VA, USA, and was a Senior Analyst with Metron, Inc., Reston, VA, USA. He is currently an Associate Teaching Professor with the Department of Mechanical and Aerospace Engineering, University of California San Diego, San Diego, CA, USA. His research interests include autonomous vehicle design, control, and navigation.

Matthew Mazloff received the B.S. degree in physics from University of Vermont, in 2000, the M.S. degree in physics from University of Vermont, in 2002, and the Ph.D. degree in physical oceanography from Massachusetts Institute of Technology, in 2008.

He is a Researcher with the Oceans and Atmospheres Section, Scripps Institution of Oceanography, University of California San Diego, San Diego, CA, USA. His research interests include understanding the ocean and earth system using model observation syntheses.

Eric Terrill received the B.S. degree in structural engineering from the Applied Mechanics and Engineering Science Laboratory, University of California San Diego, San Diego, CA, USA, in 1993, and the Ph.D. degree in applied ocean sciences from the Scripps Institution of Oceanography, University of California San Diego., in 1998.

His research interests are focused on applied ocean sciences and technology development, including marine robotics, surface waves, and coastal oceanography.